Virtual Reduced-Order Model-Based Back EMF Estimation and Speed Sensorless Control for LC-Filtered PMSM Drives

Cheng Xue, *Member, IEEE*, Xuesong Wu, *Graduate Student Member, IEEE*, Yuzhuo Li, *Member, IEEE*, and Yunwei Li, *Fellow, IEEE*

***Abstract*—The installment of the LC filter at the inverter output side reshapes the sinusoidal input voltage for the motor terminal, thus, extending a longer motor lifetime. Despite this, achieving speed sensorless control remains essential for enhanced reliability and saved costs. Currently, there is limited research on the development of a speed sensorless control tailored to high-order drive scenarios due to the increased complexity and strong coupling of the system modeling, and the unaltered adoption of the prevailing general observer methodology demands a considerably large dimensional gain matrix to guarantee observability. To fill this important research gap, this article proposes a novel back-electromotive force (EMF) modeling for the permanent magnet synchronous machine drives based on the weighted current between the filter inductor current and motor stator current. This new approach converts the third-order LCL model to the first-order L case (virtual reduced-order modeling), which enables the estimation of back EMF without relying on voltage sensors. In addition, the observer designed based on the proposed virtual model not only removes the dependency on capacitor parameters but also reduces the size of the gain matrix. This further enhances the robustness of the back EMF estimation and simultaneously simplifies the design and computation of the observation algorithm. A Kalman filter observer for back EMF estimation is implemented as a case study to verify the proposed modeling. The efficacy of the proposed speed sensorless control is also evaluated under scenarios involving variations in filter and motor inductance.**

***Index Terms*—LC filter, back electromotive force (EMF) estimation, observer gain matrix, permanent magnet synchronous machine (PMSM), speed sensorless control, virtual reduced-order model.**

Received 4 November 2024; revised 16 January 2025; accepted 22 February 2025. Date of publication 4 March 2025; date of current version 14 April 2025. This work was supported by the Natural Sciences and Engineering Research Council (NSERC) of Canada. An earlier version of this paper was presented in part at the Applied Power Electronics Conference and Exposition (APEC 2024) [DOI: 10.1109/APEC48139.2024.10509143]. Recommended for publication by Associate Editor D.-C. Lee. *(Corresponding author: Cheng Xue.)*

Cheng Xue is with the School of Integrated Circuits Science and Engineering, Southwest Jiaotong University, Chengdu 611756, China (e-mail: swjtu_xc@ieee.org).

Xuesong Wu, Yuzhuo Li, and Yunwei Li are with the Department of Electrical and Computer Engineering, University of Alberta, Edmonton, AB T6G 2V4, Canada (e-mail: xuesong3@ualberta.ca; yuzhuo@ualberta.ca; yunwei.li@ualberta.ca).

Color versions of one or more figures in this article are available at https://doi.org/10.1109/TPEL.2025.3547247.

Digital Object Identifier 10.1109/TPEL.2025.3547247

I. Introduction

THE pulsewidth modulation (PWM) process in inverters involves high-frequency switching transitions and significant voltage pulse changes (high dv/dt), which pose substantial insulation risks to motor drive systems. In scenarios, such as deep underground or remote marine environments, motor drives may encounter severe over-reflection voltage surges due to impedance mismatches between long transmission cables and the motor input side [1], [2], [3], [4]. In addition, stray capacitive couplings can induce common-mode currents that accelerate the wear and heating of motor bearings [5], [6]. Moreover, the increasing use of wide-bandgap devices heightens these issues, resulting in a larger reflection coefficient and more high-frequency electromagnetic interference (EMI) noise [7].

An effective strategy to mitigate these challenges is the deployment of a filter network between the inverter output and motor input, reshaping the output voltage into a sinusoidal waveform [8], [9], [10], [11], [12], such as the LC-filtered voltage-source inverters (VSI) [10], [11], [12]. While leveraging the benefits brought by the higher-order LCL filter network composed of the inverter-side LC filter and the motor-side stator inductance, the drive system involves an increased number of state variables, which poses new challenges for controller design and the estimation of unmeasurable system variables.

Real-time speed information is essential in the motor drives to synchronize the control signal for the power electronics device [13]. However, incorporating a rotor position sensor not only increases the total cost but also diminishes system reliability. Furthermore, the accuracy of speed sensors is susceptible to signal EMI and potential faults. Hence, the adoption of speed sensorless operation becomes indispensable, especially in challenging industrial settings where installing speed sensors is either impossible or constrained by spatial limitations. So far, speed sensorless control has been extensively researched for first-order drive systems [13], [14], [15], [16], with these methods typically categorized by their operational speed range. Unlike simpler first-order physical principles, integrating LC filters adds high-order properties to motor drives and introduces complex coupling dynamics, making sensorless speed estimation more challenging. The saliency-based sensorless control for the low-speed range is typically implemented through high-frequency signal injection [15]. This approach has been

implemented in [17] for permanent magnet synchronous machine (PMSM) drives equipped with the output LC filter, and the excitation frequency of the signal injection must be carefully selected to avoid exciting the filter resonance. On the other hand, the model-based sensorless control is developed mainly for the medium and high-speed range, and the observers for estimating the variable with position information contained have been well-established in the first-order drive system [15]. The estimation can be designed for back-electromotive force (EMF) and the motor flux for surfaced PMSM (SPMSM), or the general extended EMF [18] and active flux [19] for interior PMSM (IPMSM). However, due to the substantially distinct third-order model of the LC-filtered motor drives and limited measurement of state variables, the direct application of the aforementioned observers to medium and high-speed ranges faces significant challenges.

For example, the simple pure integrator for active flux estimation is implemented in [20] for the field-oriented control (FOC) of IPMSM with a sine-wave filter. However, high performance cannot be achieved because the author roughly uses the inverter voltage pulse and the inverter-side current to replace the motor terminal voltage and stator current, respectively, with the ignorance of the shunt capacitor. Similarly, Bu et al. [21] adopted low-pass filters to directly calculate the back EMF of SPMSM without considering the accuracy. Besides, Xu et al. [22] modeled the accurate dynamic of both SPMSM and the incorporated LC filter, and the sliding mode observer is designed to estimate the back EMF. However, the estimation relying on a third-order model necessitates a high-dimensional gain matrix, thereby increasing both tuning complexity and computational costs. A similar issue arises in the LC-filtered induction machine (IM) drive [23], where the Lunenbeger observer is employed to estimate numerous unknown variables using multiple sets of observer gains. The speed sensorless control with the measurement of both inverter-side current and motor current has been implemented in [24] for the LC-filtered IM drive, where the active damping (AD) function is incorporated simultaneously with voltage sensorless benefit. However, the reliance on pure integration operations to estimate the stator flux raises significant practical concerns, such as the dc drift and suboptimal performance in the presence of disturbances. These controller cases either ignore the dynamic effect of the LC filter and estimate the back EMF/flux roughly or introduce high complexity for both observer design and computation stage based on the high-order modeling.

Until now, the existing studies rarely developed satisfactory model-based speed sensorless control schemes tailored to high-order motor drives by combining the specific dynamic of the passive LC filter due to the aforementioned challenges. To address this critical research concern, this work takes into account the characteristics of the LC filter and develops a novel speed sensorless scheme. The primary contribution of this work lies in the proposed back EMF modeling using a virtual plant, which is based on the weighted current between the filter inductor current and the motor stator current. As a result, the back EMF estimation effectively makes the third-order model equivalent to a simple virtual first-order model with a pure L filter equivalent. The reduction in system order, previously utilized for simplifying AD controller design [25], is further advanced in this paper. The contributions of the proposed virtual modeling-based speed sensorless control can be summarized as follows.

1) The proposed system order reduction simplifies the estimation of unknown states and offers a novel approach to enhancing speed sensorless control for PMSM drives, particularly in the IPMSM case leveraging extended EMF-based estimation.
2) The proposed modeling approach enables the direct adoption of well-established back-EMF estimation strategies in LC-filtered motor drives, offering the advantage of a low-dimensional gain matrix for observer implementation, thereby significantly simplifying both the design and computation processes.
3) The proposed method avoids the dependence on capacitor parameters required by conventional sensorless approaches based on the original model, thereby enhancing the robustness of the back-EMF estimation. The proposed method also shows a higher stability margin when addressing inductance mismatch.
4) The proposed method utilizes four current sensors to implement the AD function and facilitate speed sensorless operation. Two pairs of these sensors are dedicated to measuring the current in the inverter-side inductors and the motor stator, respectively. Therefore, the proposed control scheme operates effectively without necessitating any voltage measurements.

In addition, a case study demonstrates the speed sensorless control design based on the proposed virtual plant model, which estimates the back EMF using a Kalman filter-based observer to verify the aforementioned benefits, and the phase lock loop (PLL) is adopted to extract the speed and position information. This work expands upon our idea presented in the conference paper [26], incorporating a comprehensive AD controller design, comparisons with existing high-order modeling using IPMSM, parameter robustness and stability analysis, IPMSM-based simulation validations, and extensive experimental verifications.

The rest of this article is organized as follows. Section II presents the FOC scheme with AD function for the LC-filtered PMSM drive. Section III proposes the virtual plant-based EMF modeling; A Kalman filter-based observer is then designed for the EMF estimation with detailed tuning procedures and robustness analysis. Section IV presents the simulation and experimental results to validate the proposed speed sensorless operation. Finally, Section V concludes this article.

II. AD Controller for LC-Filtered PMSM Drives

This section introduces the FOC scheme for LC-filtered PMSM drives, which is formulated within the dq coordinate frame. Fig. 1 shows the main configuration of the VSI-fed PMSM drive system, where the LC filter is connected at the inverter-side output terminal. The filter inductance is denoted as L_f and includes a parasitic resistance R_f, while the filter capacitance is represented by C_f. The three-phase inverter-side

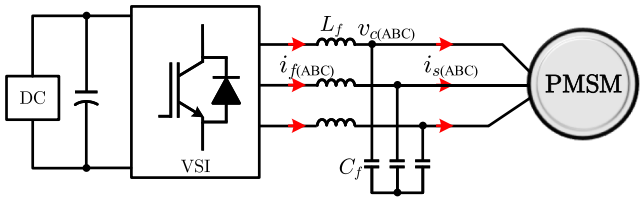

Fig. 1. Circuit diagram of the VSI-fed PMSM drive with an output LC filter.

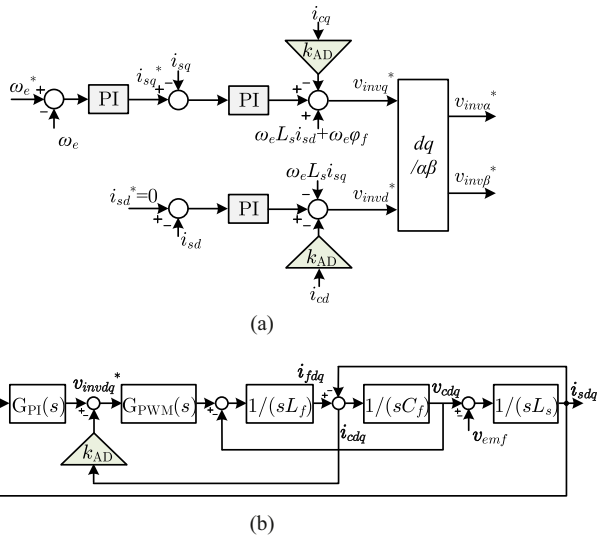

Fig. 2. FOC scheme with AD function. (a) Control loops. (b) Block diagram.

current, filter capacitor voltage, and the current flowing into the motor stator are defined as $\boldsymbol{i_{f(\mathrm{ABC})}}$, $\boldsymbol{v_{c(\mathrm{ABC})}}$, and $\boldsymbol{i_{s(\mathrm{ABC})}}$, respectively. The three-phase state variables can be transformed into the synchronous dq coordinate and two-phase stationary $\alpha\beta$ coordinate through Parks' or Clarke's transformation.

The AD function with different feedback of state variables has been well investigated on the grid side [27], [28] and the motor side [24], [29]. By emulating the dampened resistor in series or parallel with the filter component, the resonance oscillations can be effectively suppressed. This article incorporates proportional capacitor current feedback to enable the AD function, with the control loop configuration depicted in Fig. 2(a). Here, i_{sd}^* and i_{sq}^* are the dq-axes current references, and $v_{\mathrm{inv}d}^*$ and $v_{\mathrm{inv}q}^*$ are the resulting dq-axes control laws, which are subsequently transformed into the $\alpha\beta$ frame as $v_{\mathrm{inv}\alpha}^*$ and $v_{\mathrm{inv}\beta}^*$. In addition, i_{fd} and i_{fq} represent the inverter-side current components on the dq-axes, while v_{cd} and v_{cq} are the capacitor voltage components on the dq-axes. The motor stator currents on the dq-axes are denoted as i_{sd} and i_{sq}. The synchronous electrical angular velocity is represented by ω_e, L_s is the motor inductance, and ψ_f represents the permanent magnet flux linkage. The proportional capacitor current feedback makes it easier to implement the AD function compared to the capacitor voltage feedback manner, which requires a derivative operation and extra voltage sensors [28]. The dual proportional–integrator (PI) loops regulate the dq-axes motor current, and the feedforward component voltage component is added with enhanced dynamic. In addition, the dq-axes capacitor current components, i_{cd} and i_{cq}, times the damping coefficient k_{AD} individually, which are then subtracted from the output of the PI regulator. The parameter design of the PI regulator can adopt the set of values for the cases without an LC filter [25], [30]. Based on the cutoff angular frequency ω_c of the current loop, the proportional and integral gains can be respectively adopted as $k_p = L_s\omega_c$ and $k_i = R_s\omega_c$ according to the optimum criteria. Moreover, the coefficient k_{AD} should be designed to provide sufficient damping capabilities while avoiding excessive voltage decreases. The block diagram of the controller is presented in Fig. 2(b), where variables with the subscript dq are the vector forms of the previously defined variables in the dq coordinate system. Besides, the transfer function of the PI regulator and the PWM block are represented as follows:

$$G_{\mathrm{PI}}(s) = k_p + \frac{k_i}{s} \tag{1}$$

$$G_{\mathrm{PWM}}(s) = e^{-1.5T_s s}. \tag{2}$$

The digital realization of the control scheme adopts the single-update mode, where the triggers of signal sampling and control input update are operated only at the valley of the triangular carrier. Therefore, the $1.5T_s$ delay is typically assumed in the digital control, and it includes the one sampling period of computation delay and half sampling period delay caused by the discrete PWM process. It is also worth mentioning that all of the internal resistive damping has been ignored to consider the worst-case undamped scenario [31]. Based on (1) and (2), and by applying Kirchhoff voltage and current laws, the open-loop transfer function is derived as follows:

$$G_{\mathrm{open}}(s) = \frac{k_p s + k_i}{(1+sT_d)[s^4 L_s L_f C_f + s^3 k_{\mathrm{AD}} L_s C_f + s^2(L_f + L_s)]}. \tag{3}$$

The damping coefficient k_{AD} can be deliberately selected as follows to attain an equivalent damping effect as that of a physical resistor [32], i.e.,

$$k_{\mathrm{AD}} = R_{\mathrm{AD}} \frac{L_f + L_s}{L_s}. \tag{4}$$

Generally, the value of R_{AD} can be selected based on the following relationship:

$$R_{\mathrm{AD}} = \frac{1}{3 \times 2\pi f_{\mathrm{res}} C_f} \tag{5}$$

where f_{res} is the resonant frequency. In addition, it should be noted that the controller is designed based on the estimated parameters of the motor. For an IPMSM, the distinct d- and q-axes inductances can be considered separately when determining the resonance damping feedback coefficient.

III. Proposed Virtual Plant-Based Back EMF Modeling and Speed Sensorless Control

The direct state estimation for a high-order system necessitates a high dimensional gain matrix to accommodate a larger number of states and complex dynamics, which notably amplifies the challenges of tuning and computational complexity

for speed sensorless operation. This section first elucidates the design challenges of EMF observation starting from the original third-order model and then introduces the proposed virtual reduced-order model, thereby facilitating a more intuitive and comparative understanding of the contributions offered by the proposed method.

A. Back EMF Estimation and Challenges Based on Original High-Order Modeling

This article develops speed sensorless operation under the stationary $\alpha\beta$ coordinate system. To begin, the dynamic equation of the inverter-side inductor current and capacitor voltage under $\alpha\beta$ coordinate system is expressed as follows:

$$\begin{bmatrix} \frac{di_{f\alpha}}{dt} \\ \frac{di_{f\beta}}{dt} \end{bmatrix} = \begin{bmatrix} -\frac{R_f}{L_f} & 0 \\ 0 & -\frac{R_f}{L_f} \end{bmatrix} \begin{bmatrix} i_{f\alpha} \\ i_{f\beta} \end{bmatrix} + \begin{bmatrix} \frac{1}{L_f} & 0 \\ 0 & \frac{1}{L_f} \end{bmatrix} \begin{bmatrix} v_{\text{inv}\alpha} - v_{c\alpha} \\ v_\beta - v_{c\beta} \end{bmatrix} \tag{6}$$

$$\begin{bmatrix} \frac{dv_{c\alpha}}{dt} \\ \frac{dv_{c\beta}}{dt} \end{bmatrix} = \begin{bmatrix} \frac{1}{C_f} & 0 \\ 0 & \frac{1}{C_f} \end{bmatrix} \begin{bmatrix} i_{f\alpha} - i_{s\alpha} \\ i_{f\beta} - i_{s\beta} \end{bmatrix}. \tag{7}$$

Further, according to the extended EMF equation for IPMSM [18], the dynamic of the motor stator current under the $\alpha\beta$ coordinate can be reformulated as follows:

$$\begin{bmatrix} \frac{di_{s\alpha}}{dt} \\ \frac{di_{s\beta}}{dt} \end{bmatrix} = \begin{bmatrix} -\frac{R_s}{L_{sd}} & 0 \\ 0 & -\frac{R_s}{L_{sd}} \end{bmatrix} \begin{bmatrix} i_{s\alpha} \\ i_{s\beta} \end{bmatrix} + \begin{bmatrix} \frac{1}{L_{sd}} & 0 \\ 0 & \frac{1}{L_{sd}} \end{bmatrix} \begin{bmatrix} v_{c\alpha} \\ v_{c\beta} \end{bmatrix} + \frac{v_{\text{eemf}}}{L_{sd}} \begin{bmatrix} \sin\theta_e \\ -\cos\theta_e \end{bmatrix} + \omega_e \frac{L_\Delta}{L_{sd}} \begin{bmatrix} -i_{s\beta} \\ i_{s\alpha} \end{bmatrix} \tag{8}$$

where R_s denotes the stator resistance, and L_{sd} and L_{sq} represent the stator inductances on the dq-axes, respectively. For the SPMSM case, the dq-axes inductances are equal, i.e., $L_{sd} = L_{sq} = L_s$. Here, $L_\Delta = L_{sd} - L_{sq}$ indicates the inductance difference between the dq-axes caused by the saliency of IPMSM. Besides, the electrical position angle is denoted by θ_e, and the extended back EMF magnitude, v_{eemf}, is expressed as $v_{\text{eemf}} = (L_d - L_q)(\omega_e i_{sd} - di_{sq}/dt) + \omega_e \psi_f$. Based on (6) through (8), the LC-filtered motor drives are characterized by third-order dynamics with significant coupling among the state variables. The dynamic equations of LC-filtered motor drives in matrix form is further expressed as follows:

$$\frac{d\boldsymbol{x_o}}{dt} = \mathbf{A_o}\boldsymbol{x_o} + \mathbf{B_o}\boldsymbol{u} + \mathbf{E_o} \tag{9}$$

where the state vector $\boldsymbol{x_o} = [i_{f\alpha}\ i_{f\beta}\ v_{c\alpha}\ v_{c\beta}\ i_{s\alpha}\ i_{s\beta}]^{\text{T}}$ and the input voltage vector $\boldsymbol{u} = [v_{\text{inv}\alpha}\ v_{\text{inv}\beta}]^{\text{T}}$. The system matrix $\mathbf{A_o}$, $\mathbf{B_o}$, and $\mathbf{E_o}$ are given in Appendix A. Here, it should be noted that the matrix $\mathbf{A_o}$ has dimensions of 6×6, $\mathbf{B_o}$ is 6×2, and $\mathbf{E_o}$ is 6×1. Assuming that the time length of the sampling interval is T_s, and the current time step is k, the modeling (9) in the discretized domain can be obtained based on the zero-order-hold

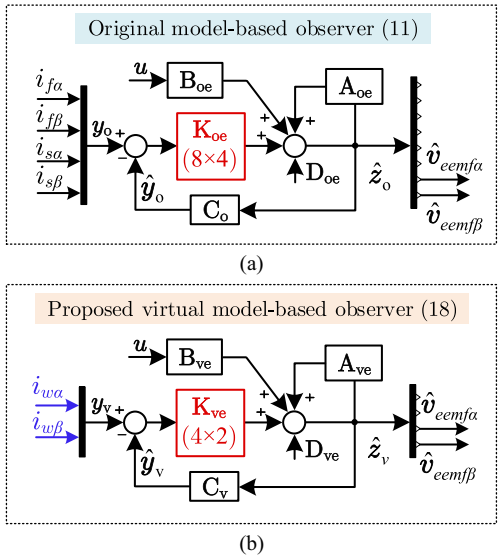

Fig. 3. Comparative visualization of back EMF estimation observers for speed sensorless control. (a) Observer design (11) based on the original high-order model. (b) Observer design (18) based on the proposed virtual reduced-order model.

(ZOH) principle, i.e.,

$$\boldsymbol{x_o}(k+1) = \mathbf{A_{od}}\boldsymbol{x_o}(k) + \mathbf{B_{od}}\boldsymbol{u}(k) + \mathbf{E_{od}} \tag{10}$$

where the discrete matrice are calculated using the first-order Euler discretization, i.e., $\mathbf{A_{od}} = \mathbf{I} + \mathbf{A_o}T_s$, $\mathbf{B_{od}} = \mathbf{B_o}T_s$ and $\mathbf{E_{od}} = \mathbf{E_o}T_s$. Based on (10), commonly used observers, such as Kalman filter type, can be employed to perform online estimation of the extended back EMF in matrix $\mathbf{E_o}$, which includes positional angle information. Assuming that the dynamics of the back EMF evolve more slowly than the rapid sampling process, the observer formulation based on the original third-order model can be expressed as follows:

$$\begin{cases} \hat{\boldsymbol{z_o}}(k+1) = \mathbf{A_{oe}}\hat{\boldsymbol{z_o}}(k) + \mathbf{B_{oe}}\boldsymbol{u}(k-1) \\ \qquad\qquad +\mathbf{K_{oe}}\left[\boldsymbol{y_o}(k) - \hat{\boldsymbol{y_o}}(k)\right] + \mathbf{D_{oe}} \\ \boldsymbol{y_o}(k) = \mathbf{C_o}\boldsymbol{z_o}(k) \\ \hat{\boldsymbol{y_o}}(k) = \mathbf{C_o}\hat{\boldsymbol{z_o}}(k) \end{cases} \tag{11}$$

where the extended vector $\boldsymbol{z_o} = [i_{f\alpha}\ i_{f\beta}\ v_{c\alpha}\ v_{c\beta}\ i_{s\alpha}\ i_{s\beta}\ v_{\text{eemf}\alpha}\ v_{\text{eemf}\beta}]^{\text{T}}$ and the output vector $\boldsymbol{y_o} = [i_{f\alpha}\ i_{f\beta}\ i_{s\alpha}\ i_{s\beta}]^{\text{T}}$. The vectors $\hat{\boldsymbol{z_o}}$ and $\hat{\boldsymbol{y_o}}$ represent the estimation information of $\boldsymbol{z_o}$ and $\boldsymbol{y_o}$, respectively. The matrices are expressed as follows:

$\mathbf{A_{oe}} = \begin{bmatrix} \mathbf{A_{od}} & \mathbf{Z} \\ \mathbf{0}_{2\times6} & \mathbf{0}_{2\times2} \end{bmatrix}$, $\mathbf{B_{oe}} = \begin{bmatrix} \mathbf{B_{od}} \\ \mathbf{0}_{2\times2} \end{bmatrix}$, and $\mathbf{Z} = \begin{bmatrix} \mathbf{0}_{4\times2} \\ \frac{1}{L_{sd}}\mathbf{I}_{2\times2} \end{bmatrix}$, $\mathbf{D_{oe}} = [0\ 0\ 0\ 0\ \frac{-T_s\omega_e L_\Delta i_{s\beta}}{L_{sd}}\ \frac{T_s\omega_e L_\Delta i_{s\alpha}}{L_{sd}}\ 0\ 0]^{\text{T}}$, where $\mathbf{I_{2\times2}}$ is the second order identity matrix. Fig. 3(a) visually illustrates the back EMF estimation based on the original model. The currents $i_{f\alpha}$, $i_{f\beta}$, $i_{s\alpha}$, and $i_{s\beta}$, which are the actual measured values and serve as the output variables, enable the estimation of back EMF when the observer achieves convergence.

Therefore, it can be seen that to facilitate the implementation of the observer based on the original third-order model, the dimension of the gain matrix $\mathbf{K_{oe}}$ should be 8×4. Consequently, the large size of $\mathbf{K_{oe}}$ complicates the design and particularly the computational process during real-time updates. Moreover, the estimation stage involves the capacitor parameters C_f in addition to inductor parameters.

B. Proposed Virtual-Plant-Based Back EMF Modeling for IPMSM

The proposed modeling suits both the IPMSM and SPMSM with the extended EMF equation-based derivation. The proposed virtual plant turns the order of the drive system from third to first. Therefore, the dimension of the observer gain matrix can be significantly reduced, which facilitates an easy adoption of the advanced EMF estimation approach. In addition, the proposed method operates independently of capacitor parameters and offers voltage-sensorless advantages.

Compared (6) with (8), it can be seen that the dynamic of both the inverter-side inductor current and the stator current are related to the filter capacitor voltage. To avoid reliance on any voltage measurement, it is feasible to neutralize the effect of capacitor voltage as the sign of the capacitor voltage in (6) and (8) are opposite. To this end, a weighted average current under the stationary coordinate can be defined as follows [25]:

$$\begin{bmatrix} i_{w\alpha} \\ i_{w\beta} \end{bmatrix} = \frac{L_f}{L_f + L_{sd}} \begin{bmatrix} i_{f\alpha} \\ i_{f\beta} \end{bmatrix} + \frac{L_{sd}}{L_f + L_{sd}} \begin{bmatrix} i_{s\alpha} \\ i_{s\beta} \end{bmatrix}. \tag{12}$$

It can be seen that this current is the weighted sum of these two currents, and the weights assigned are determined by the respective proportions of the filter inductance or motor inductance in the total inductance value. Further, based on the definition of the weighted current in (12), its dynamic equation can be readily derived by substituting the aforementioned dynamic equations of the filter current (6) and the motor current (8), which is expressed as follows:

$$\begin{aligned} \begin{bmatrix} \frac{di_{w\alpha}}{dt} \\ \frac{di_{w\beta}}{dt} \end{bmatrix} &= \begin{bmatrix} -k_{R/L} & 0 \\ 0 & -k_{R/L} \end{bmatrix} \begin{bmatrix} i_{w\alpha} \\ i_{w\beta} \end{bmatrix} \\ &+ \begin{bmatrix} \frac{1}{L_f+L_{sd}} & 0 \\ 0 & \frac{1}{L_f+L_{sd}} \end{bmatrix} \begin{bmatrix} v_{\text{inv}\alpha} \\ v_{\text{inv}\beta} \end{bmatrix} \\ &+ \frac{v_{\text{eemf}}}{L_f+L_{sd}} \begin{bmatrix} \sin\theta_e \\ -\cos\theta_e \end{bmatrix} + \omega_e \frac{L_\Delta}{L_f+L_{sd}} \begin{bmatrix} -i_{s\beta} \\ i_{s\alpha} \end{bmatrix}. \end{aligned} \tag{13}$$

It can be seen that the presented (13) closely resembles the dynamics of current flowing through a first-order inductor L_{s_virtual} when voltage is applied across its two terminals and $L_{s\_\text{virtual}} = L_f + L_{sd}$. It should be noticed that $k_{R/L}$ represents the equivalent resistance to inductance ratio of L_{s_virtual}, and the assumption that $R_s/L_s = R_f/L_f = k_{R/L}$ is made during the derivation process. This assumption is made with deliberation, and it is especially reasonable in the context of an extreme scenario where both the resistance of the filter inductance and the motor inductance are neglected as zero [31]. In addition, during the discretization process, the corresponding values of both 1-R_sT_s/L_s and 1-R_fT_s/L_f become so small that it is feasible to assume they are equal and reasonable to disregard them altogether. Therefore, this assumption has an insignificant impact on the dynamics of the proposed virtual model yet guarantees that it exhibits the characteristics of a first-order inductor, thereby enhancing the physical interpretability of the proposed reduced-order process.

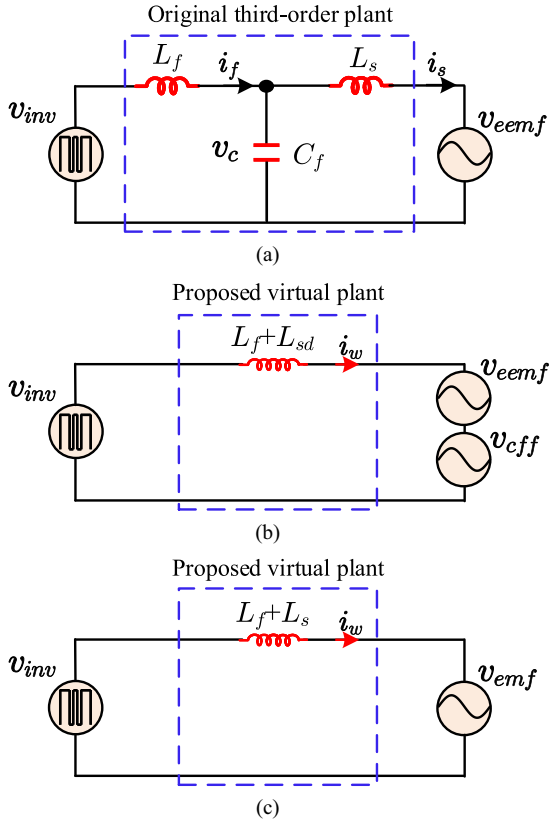

Fig. 4. Comparison between conventional third-order modeling and proposed first-order virtual plant for LC-filtered PMSM drives. (a) Per-phase circuit of conventional third-order modeling. (b) Per-phase circuit of the proposed first-order modeling for IPMSM with LC filter. (c) Per-phase circuit of the proposed first-order modeling for SPMSM with LC filter.

The additional voltage component shown in (13) is denoted by v_{cff}, and its $\alpha\beta$ component is expressed as follows:

$$\begin{bmatrix} v_{\text{cff}\alpha} \\ v_\beta \end{bmatrix} = \omega_e L_\Delta \begin{bmatrix} -i_{s\beta} \\ i_{s\alpha} \end{bmatrix}. \tag{14}$$

The component v_{cff} exists due to the saliency property of IPMSM. Notably, the proposed modeling (13) eliminates the dynamic of the filter capacitor voltage and thus builds the connections between the inverter output voltage and the back EMF directly through the dynamic of weighted current. As a result, the system can be reduced from the original third-order model to the virtual first-order one. Fig. 4 presents the modeling relationships to facilitate the intuitive analysis of the reduced-order process [33]. The per-phase equivalent circuit in Fig. 4(a) represents the original third-order motor drive, where the inverter-side current, capacitor voltage, and stator current are coupled with the inverter output voltage as the control input. The first-order per-phase equivalent circuit in Fig. 4(b) stands

for the derived modeling given in (13). The control input voltage is directly connected with the back EMF and additional voltage component through the virtual inductor, whose value is L_f+L_{sd}. Therefore, the proposed virtual modeling is significantly simplified compared to the original one.

C. Proposed Virtual First-Order Modeling for SPMSM Case

Given the symmetry of the SPMSM, characterized by identical d- and q-axes inductances, the virtual model established in (13) can be further simplified. Namely, under the SPMSM case with $L_\Delta = 0$, the additional voltage component $\boldsymbol{v}_{\text{cff}}$ given in (14) equals zero, and thus (13) fully turns to the expression about the dynamic of stator current, simulating the presence of a motor with virtual stator inductance $L_{s\_\text{virtual}} = L_f + L_s$, i.e.,

$$\begin{aligned}\begin{bmatrix}\frac{di_{w\alpha}}{dt}\\ \frac{di_{w\beta}}{dt}\end{bmatrix} &= \begin{bmatrix}-k_{R/L} & 0\\ 0 & -k_{R/L}\end{bmatrix}\begin{bmatrix}i_{w\alpha}\\ i_{w\beta}\end{bmatrix}\\ &+\begin{bmatrix}\frac{1}{L_{s\_\text{virtual}}} & 0\\ 0 & \frac{1}{L_{s\_\text{virtual}}}\end{bmatrix}\begin{bmatrix}v_{\text{inv}\alpha}\\ v_\beta\end{bmatrix}\\ &+\frac{v_{emf}}{L_{s\_\text{virtual}}}\begin{bmatrix}\sin\theta_e\\ -\cos\theta_e\end{bmatrix}\end{aligned} \tag{15}$$

where $v_{\text{emf}} = \omega_e\psi_f$ represents the back EMF of SPMSM. Particularly, for the SPMSM case, the virtual plant modeling is presented in Fig. 4(c) without the additional voltage item $\boldsymbol{v}_{\text{cff}}$. Consequently, the system can be fully equivalent to the VSI-fed SPMSM case without the LC filters, where the virtual stator inductance of the SPMSM can be deemed as L_f+L_s to maintain equivalence.

D. Virtual Plant-Based Kalman Filter Observer for Back EMF Estimation

Utilizing the first-order property of the proposed virtual plant facilitates the development of advanced observers for EMF estimation. The reduced complexity of the virtual plant significantly lowers the dimension of the feedback gain matrix required in the closed-loop observer, and capacitance values are not needed during the estimation stage. To implement these enhancements, the extended model for observer formulation is presented as follows:

$$\frac{d\boldsymbol{z_v}}{dt} = \mathbf{A_v}\boldsymbol{z_v} + \mathbf{B_v}\boldsymbol{u} + \mathbf{D_v} \tag{16}$$

where the extended vector $\boldsymbol{z_v} = [i_{w\alpha}\ i_{w\beta}\ v_{\text{eemf}\alpha}\ v_{\text{eemf}\beta}]^{\text{T}}$ and the matrice can be expressed as follows according to (13):

$$\mathbf{A_v} = \begin{bmatrix}-k_{R/L} & 0 & \frac{1}{L_{s\_\text{virtual}}} & 0\\ 0 & -k_{R/L} & 0 & \frac{1}{L_{s\_\text{virtual}}}\\ 0 & 0 & 0 & 0\\ 0 & 0 & 0 & 0\end{bmatrix},$$

$$\mathbf{B_v} = \begin{bmatrix}\frac{1}{L_{s\_\text{virtual}}} & 0\\ 0 & \frac{1}{L_{s\_\text{virtual}}}\\ 0 & 0\\ 0 & 0\end{bmatrix}, \text{ and}$$

$$\mathbf{D_v} = [\tfrac{-\omega_e L_\Delta i_{s\beta}}{L_{s\_\text{virtual}}}\ \ \tfrac{\omega_e L_\Delta i_{s\alpha}}{L_{s\_\text{virtual}}}\ \ 0\ \ 0]^{\text{T}}.$$

The modeling (16) in the discretized domain can be then obtained based on the ZOH principle, i.e.,

$$\boldsymbol{z_v}(k+1) = \mathbf{A_{ve}}\boldsymbol{z_v}(k) + \mathbf{B_{ve}}\boldsymbol{u}(k) + \mathbf{D_{ve}} \tag{17}$$

where the discrete matrice are calculated using the first-order Euler discretization, i.e., $\mathbf{A_{ve}} = \mathbf{I} + \mathbf{A_v}T_s$ and $\mathbf{B_{ve}} = \mathbf{B_v}T_s$, $\mathbf{D_{ve}} = \mathbf{D_v}T_s$. To estimate the information of EMF, the discrete Kalman-filter-based observer is designed as follows:

$$\begin{cases}\hat{\boldsymbol{z_v}}(k+1) = \mathbf{A_{ve}}\hat{\boldsymbol{z_v}}(k) + \mathbf{B_{ve}}\boldsymbol{u}(k-1)\\ \qquad\qquad +\mathbf{K_{ve}}\left[\boldsymbol{y_v}(k) - \hat{\boldsymbol{y_v}}(k)\right] + \mathbf{D_{ve}}\\ \boldsymbol{y_v}(k) = \mathbf{C_v}\boldsymbol{z_v}(k)\\ \hat{\boldsymbol{y_v}}(k) = \mathbf{C_v}\hat{\boldsymbol{z_v}}(k)\end{cases} \tag{18}$$

where $\hat{\boldsymbol{z_v}} = [\hat{i}_{w\alpha}\ \hat{i}_{w\beta}\ \hat{v}_{emf\alpha}\ \hat{v}_{emf\beta}]^{\text{T}}$ is the estimated state vector and the matrix $\mathbf{C_v}$ is given by $\mathbf{C_v} = \left[\begin{smallmatrix}1&0&0&0\\0&1&0&0\end{smallmatrix}\right]$. The output vector $\boldsymbol{y_v} = [i_{w\alpha}\ i_{w\beta}]^{\text{T}}$, and its estimated counterpart is $\hat{\boldsymbol{y_v}} = [\hat{i}_{w\alpha}\ \hat{i}_{w\beta}]^{\text{T}}$. It should be noted that the observer design considers the one-step digital delay, where the input voltage $\boldsymbol{u}(k\text{-}1)$ computed from the last control interval will be applied at the k instant. Therefore, the estimation of EMF is implemented in the one-step forward prediction manner, which effectively compensates for the digital delay effect in the closed-loop sensorless operation. The feedback gain matrix $\mathbf{K_{ve}}$ can be calculated recursively according to [34]

$$\begin{cases}\mathbf{K_{ve}}(k) = \mathbf{A_{ve}}\mathbf{P}(k)\mathbf{C_{ve}}^{\text{T}}\left[\mathbf{C_{ve}}\mathbf{P}(k)\mathbf{C_{ve}}^{\text{T}} + \mathbf{R}\right]^{-1}\\ \mathbf{P}(k+1) = \mathbf{A_{ve}}\left[\mathbf{I_{4\times4}} - \mathbf{K_{ve}}(k)\mathbf{C_{ve}}\right]\mathbf{P}(k)\mathbf{A_{ve}}^{\text{T}} + \mathbf{Q}\end{cases} \tag{19}$$

where $\mathbf{I_{4\times4}}$ is the fourth order identity matrix, and $\mathbf{P}$ represents the covariance matrix for the estimated state errors. Supposing that ξ and τ represent the covariance matrices for the noise caused by modeling mismatch and measurement, respectively, the matrix $\mathbf{Q}$ and $\mathbf{R}$ can be, respectively, calculated as $\mathbf{Q} = \text{E}(\xi\xi^{\text{T}})$ and $\mathbf{Q} = \text{E}(\tau\tau^{\text{T}})$. Generally, a larger $\mathbf{Q}$ and a smaller $\mathbf{R}$ cause stronger updating of the estimated vector and thus bring a high estimated bandwidth [35]. Fig. 3(b) visually presents the back EMF estimation based on the proposed virtual model, where the difference from Fig. 3(a) can be clearly observed, as it directly uses the weighted current as the output variable. Particularly, it should be noted that the observer design outlined in (18) necessitates the use of a 4×2-dimensional gain matrix $\mathbf{K_{ve}}$, which is rooted in the utilization of the proposed simplified first-order model. However, for the original third-order model-based observer design, the size of the gain matrix $\mathbf{K_{oe}}$ given in (11) would expand to a dimension of 8×4. The proposed method significantly simplifies both the design and computational stages.

E. Comparative Analysis of Parameter Mismatch in Proposed Virtual Model-Based and Original Model-Based Observers

Although the proposed virtual model is independent of the filter capacitance value, it relies on both the filter inductance and the motor stator inductance to mitigate the dynamics of the capacitor voltage. Hence, it is necessary to check the robustness

performance of the observer in the case of filter inductance and motor stator inductance mismatch. Defining the error of the estimated state as $\tilde{\boldsymbol{z}}_{\boldsymbol{v}}(k) = \boldsymbol{z}_{\boldsymbol{v}}(k) - \hat{\boldsymbol{z}}_{\boldsymbol{v}}(k)$, the dynamic of the observer error system can be obtained according to (17) and (18), i.e.,

$$\tilde{\boldsymbol{z}}_{\boldsymbol{v}}(k+1) = \left(\mathbf{A_{ve}} - \mathbf{K_{ve}}\mathbf{C_{ve}}\right)\tilde{\boldsymbol{z}}(k). \tag{20}$$

The discrete observer, thus, achieves asymptotic stability under the condition where all eigenvalues of the closed-loop error matrix remain within the unit circle. Besides, it should be noted that the weighted current is derived from the real measurements of the inverter-side and motor-side currents, ensuring it reflects the accurate state of the actual plant model. The Kalman filter leverages the actual system feedback to iteratively refine the estimated states, ensuring convergence. While $\boldsymbol{z}_{\boldsymbol{v}}$ represents the state of the simplified virtual plant, the error term in the observer formulation is continually corrected based on the real system feedback (weighted current), which includes dynamics captured by the real system.

As time step k goes to infinity, the steady-state solutions of gain matrix (19) satisfy the discrete-time algebraic Riccati equation [34], i.e.,

$$\begin{cases} \mathbf{K_{ve}}(\infty) = \mathbf{A_{ve}}\mathbf{P}(\infty)\mathbf{C_{ve}}^{\mathrm{T}}\left[\mathbf{C_{ve}}\mathbf{P}(\infty)\mathbf{C_{ve}}^{\mathrm{T}} + \mathbf{R}\right]^{-1} \\ \mathbf{P}(\infty) = \mathbf{A_{ve}}\left[\mathbf{I_{4\times4}} - \mathbf{K_{ve}}(\infty)\mathbf{C_{ve}}\right]\mathbf{P}(\infty)\mathbf{A_{ve}}^{\mathrm{T}} + \mathbf{Q}. \end{cases} \tag{21}$$

In this case, the Kalman filter gain $\mathbf{K_{ve}}$ can be solved using the *dare* command in Matlab. In the study, the matrices of $\mathbf{Q}$ and $\mathbf{R}$ are, respectively, designed as diag(0.0001, 0.0001, 0.01, 0.01) and diag(0.0001, 0.0001) considering the closed-loop convergence speed and the disturbance rejection ability. This article adopts a set of IPMSM parameters, including $R_s = 12.4$ m Ω, $L_{sd} = 0.8$ mH, $L_{sq} = 1.6$ mH, $\psi_f = 0.0934$ Wb as well as the filter parameters are $L_f = 1$ mH, $C_f = 30$ μ F. Under the case of 10 kHz sampling frequency, the Kalman gain matrix $\mathbf{K_{oe}}$ and $\mathbf{K_{ve}}$ as required in conventional observers (11) and proposed (18) can be computed, where the results have been given in Appendix B.

Fig. 5 depicts the closed-loop pole map of the observer as system parameters deviate, and it features comparisons between estimation cases using the original third-order model and the proposed virtual reduced-order model. Fig. 5(a) and (b), respectively, shows the root loci of observers based on the original model and the proposed model as the filter inductance L_f varies from 50% to 150% of the actual inductance value. It is evident that the observer based on the original model becomes unstable when the filter inductance L_f is reduced to 50% of its actual value. In contrast, the observer using the proposed virtual reduced-order model always remains stable under the $\pm$ 50% mismatch range of filter inductance. Similarly, the root loci of observers based on these two models under the $\pm$ 50% mismatch range of motor inductance are presented in Fig. 5(c) and (d), respectively. The original model-based observer exhibits a wider range of pole variation, with poles migrating toward the unit circle boundary when the motor inductance is lower than the actual value, resulting in a reduced stability margin. Conversely, the proposed model-based observer demonstrates a narrower

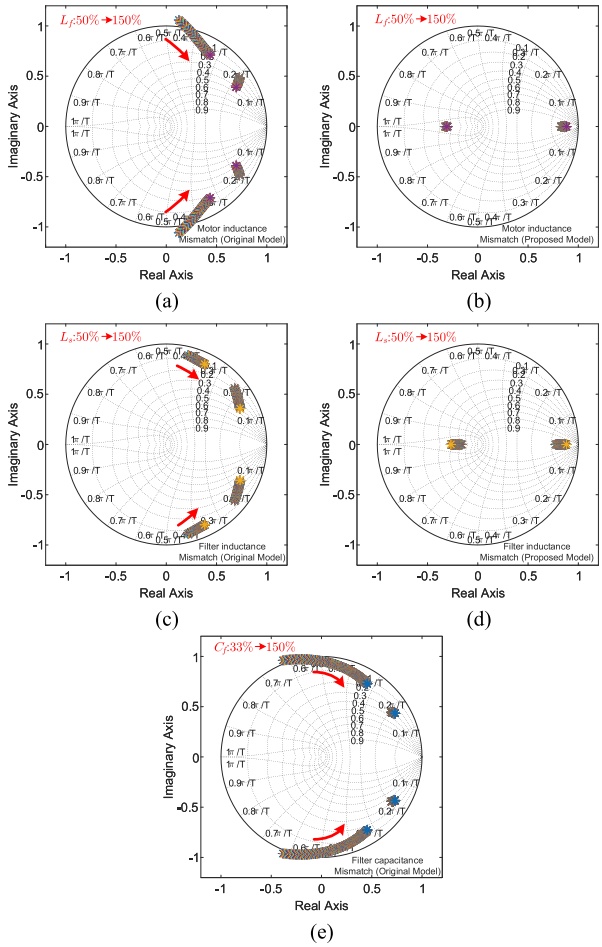

Fig. 5. Root loci of the closed-loop observer poles with the parameter variation of (a) original model-based observer under filter inductance mismatch. (b) Proposed virtual model-based observer under filter inductance mismatch. (c) Original model-based observer under motor inductance mismatch. (d) Proposed virtual model-based observer under motor inductance mismatch. (e) Original model-based observer under filter capacitance mismatch.

pole variation range, and its stability is consistently guaranteed. Hence, the proposed method ensures stronger robustness than the conventional methods in terms of the filter or motor inductance mismatch. Furthermore, it is worth mentioning that the observer derived from the original model depends on parameters associated with the filtering capacitor. From Fig. 5(e), it can be observed that when the filtering capacitor value is reduced to 33% of the actual value, the observer becomes unstable. In contrast, the proposed observer does not face this challenge, as it operates on a first-order model characterized by reduced coupling and independence from filtering capacitor parameters.

In addition to stability analysis of the observer under parameter mismatch conditions, the impact of inductance mismatch on back EMF observation can be intuitively analyzed through the proposed virtual reduced-order model. Considering the discrepancy in the inductance value used in the computation stage of the controller, an additional virtual inductance will be introduced into the control loop, as illustrated in the equivalent circuit depicted in Fig. 6. Either the increased mismatch of the L_f or L_s in the control scheme will introduce the virtual positive

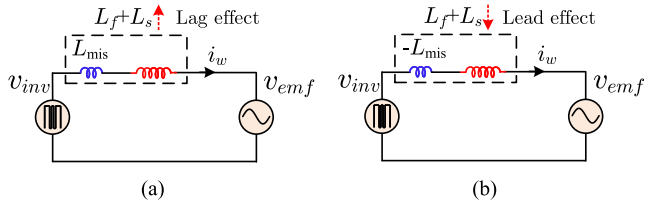

Fig. 6. Proposed reduced-order model under mismatched inductance. (a) Increased mismatch case of either L_f or L_s. (b) Reduced mismatch case of either L_f or L_s.

inductance L_{mis} ($L_{\text{mis}} = L_{\text{estimated}}$-$L_{\text{actual}}$, representing the difference between the inductance used in the controller and the real value of system), causing the phase lag effect on the estimated EMF. As a result, the estimated position information of the rotor will be delayed compared to the real position information. Conversely, a reduction in either the filter inductance L_f or the motor stator inductance L_s results in a virtual negative inductance L_{mis}, leading to a phase lead effect on the estimated EMF, which consequently, causes the estimated rotor position information to advance relative to the actual information.

IV. Simulation and Experimental Verification

The overall implementation of the proposed virtual plant-based speed sensorless operation is presented in Fig. 7. The FOC scheme with AD function (see Fig. 2) is implemented with the estimated speed information instead of using the real sensor-based measurement. The controller operates in speed control mode, utilizing an outer PI loop to maintain precise speed command tracking and produce the current magnitude reference. The maximum torque per ampere principle is adopted to compute the d-axis and q-axis current, where the optimum current vector angle is calculated for IPMSM [36] and $i_d^* = 0$ can be directly set for the SPMSM case. The inverter-side and motor stator currents are sampled in two phases, which allows the subsequent calculation of both capacitor and weighted currents derived from these measurements. The generated control voltage command will serve as the input for the Kalman filter observer to estimate the back EMF information. A type-3 synchronous reference frame-phase-locked loop [37] is adopted to extract the real-time speed and position information from the estimated back EMF. Incidentally, the proposed back EMF observer in Fig. 7 corresponds to Fig. 3(b). The sensorless control based on the original model is achieved by replacing the observer in Fig. 7 with the one in Fig. 3(a), while keeping the rest unchanged.

A. Simulation Verification

To validate the correctness and effectiveness of the proposed virtual reduced-order model in IPMSM applications, simulation test results based on MATLAB Simulink are conducted. The key IPMSM parameters includes $R_s = 12.4$ m Ω, $L_{sd} = 0.8$ mH, $L_{sq} = 1.6$ mH, $\psi_f = 0.0934$ Wb, among others, including dc-link voltage $V_{\text{dc}} = 380$ V, switching frequency $f_{sw} = 10$ kHz. The filter inductance is normally chosen to fulfill two objectives: suppressing switching ripple current and minimizing voltage drop across it [10]. Another guideline suggests matching the filter inductance with the motor side inductance to avoid re-designing other system parameters such as the dc-bus capacitor and heat sink [24]. The capacitance value can be determined based on the cutoff frequency of the LC filter, typically set below the switching frequency to attenuate high-frequency harmonics [28]. Here, the LC filter parameters $L_f = 1$ mH and $C_f = 30$ μ F are chosen to satisfy these requirements.

Fig. 8 presents a comparative analysis of steady-state performance between the original model-based speed sensorless control and the proposed reduced-order model, where n_r is rotor revolutions per minute of the motor, $\widetilde{n}_r$ is the estimation error of rotor speed, and $\widetilde{\theta}_e$ is the estimation error of electrical position angle. In addition, it shows the dynamic responses to a motor speed command change, where the rotor speed shifts from 1000 r/min to the rated speed of 2000 r/min. All control parameters are consistent across both scenarios. Due to the limited bandwidth, the observed back EMF experiences increased delay as the motor speed rises, leading to larger position angle errors. As shown in Fig. 8(a), this error is more pronounced and severe for the method based on the original model. The results indicate that the sensorless control using the proposed model yields lower errors in speed and phase angle estimation compared to the original model. Furthermore, since the proposed virtual model effectively minimizes the decoupling among state variables in LC-filtered motor drives, the proposed method demonstrates quicker convergence in estimating speed and phase angle. Moreover, Fig. 9 illustrates a comparison between the original model-based speed sensorless control and the proposed reduced-order model, specifically observing the transition from a no-load condition to a rated load of 10 N·m while maintaining a rotor speed of 2000 r/min. The proposed model consistently demonstrates reduced errors in speed and phase angle estimation compared to the original model-based control.

Fig. 10 demonstrates the robustness test of sensorless control using different models, where parameter changes were implemented as a gradual ramp starting at 4 s. Fig. 10(a) shows the control waveform from the original model under the ultimate -50% mismatch of filter inductance, which indicates a loss of closed-loop stability in the system. Similarly, in Fig. 10(b), the original model exhibits instability under the mismatch of the filter capacitor. The proposed virtual reduced-order model, however, does not depend on capacitor parameters and thus does not suffer from the capacitance value mismatch. In Fig. 10(c), the proposed model maintains stability under a -50% mismatch of filter inductance value, which proves the improved robustness compared to the original model, as seen in Fig. 10(a). Similarly, Fig. 10(d) shows that the proposed model remains stable even with a -50% mismatch in motor inductance value.

Fig. 11 presents the validation of the proposed virtual reduced-order model-based sensorless control for IPMSM, incorporating a nonsinusoidal back-EMF with 5% fifth and 3% seventh harmonic content to simulate an extreme scenario of high harmonic distortion. The results indicate that the proposed sensorless control model achieves reduced speed and position estimation errors

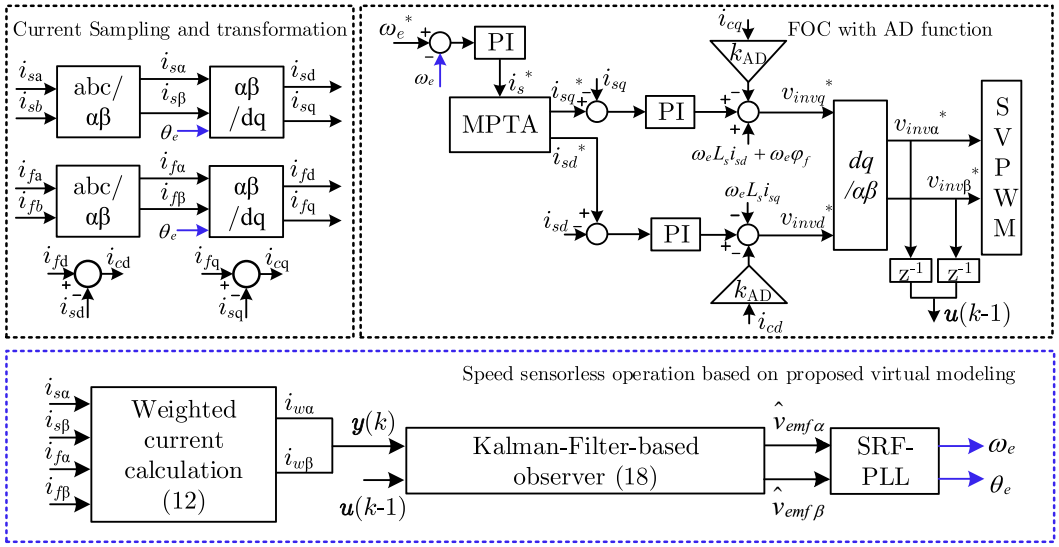

Fig. 7. Diagram of speed sensorless controller for PMSM based on proposed virtual reduced-order model.

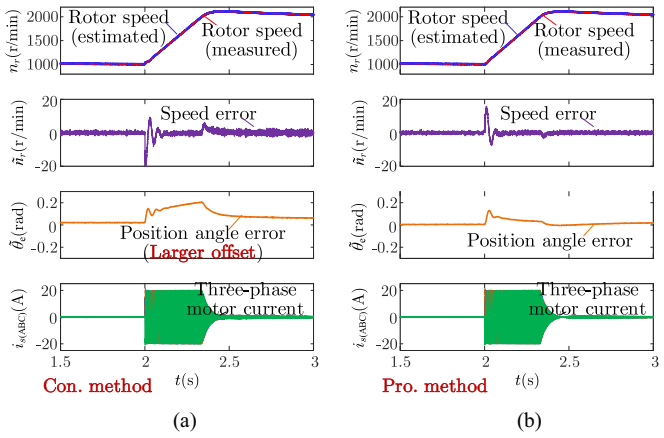

Fig. 8. Speed sensorless control performance comparison between conventional model and proposed reduced-order model under steady-state and dynamic condition (rotor speed changes from 1000 r/min to rated 2000 r/min, no-load). (a) Sensorless control based on conventional model. (b) Sensorless control based on the proposed model.

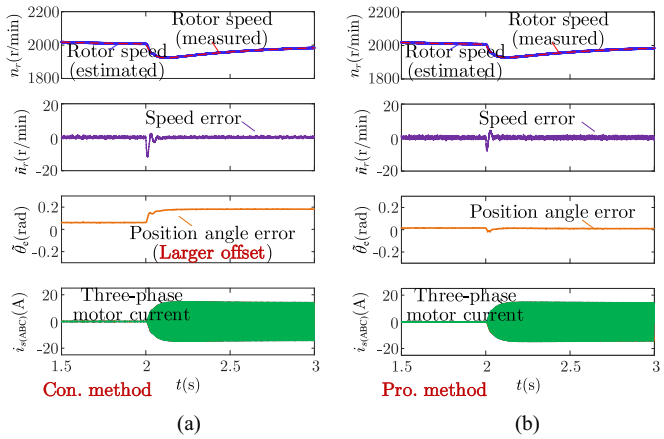

Fig. 9. Speed sensorless control performance comparison between conventional model and proposed reduced-order model under dynamic condition (load changes from 0 N·m to rated 10N· m). (a) Sensorless control based on conventional model. (b) Sensorless control based on the proposed model.

compared to the original model, demonstrating its robustness and effectiveness when applied to high-fidelity IPMSM models. However, the nonsinusoidal back-EMF introduces additional ripples in the estimated speed error, as compared to a motor with sinusoidal back-EMF. To further enhance sensorless control under the influence of fifth and seventh harmonics, established methods such as the second-order generalized integrator (SOGI)-based multiple selective EMF harmonic elimination method, as described in [38], can be integrated into the proposed virtual model to improve estimation accuracy by filtering low-order harmonics.

To evaluate the performance of the proposed algorithm in high-speed applications, Fig. 12 illustrates the results of a dynamic simulation where the motor speed was increased from 10 000 to 20 000 r/min. High-speed motors typically exhibit lower inductance, and in this simulation, both the filter inductance and the IPMSM inductances were halved. Furthermore, the dc-link voltage was increased, and the switching frequency was elevated to 20 kHz to accommodate the higher fundamental frequency at these speeds. The comparative results in Fig. 12 reveal that the sensorless control method based on the proposed virtual model outperforms the traditional model, particularly in terms of dynamic response, position angle accuracy, and convergence speed. This enhanced performance is due to the ability of the virtual model to mitigate higher order coupling effects introduced by the LC filter, even at high speeds. Although increased motor speed introduces increased delay in the observed back EMF due to the limited bandwidth of the digital controller and observer, this challenge affects both models and can be addressed by optimizing the sampling frequency and redesigning the feedback gain matrix.

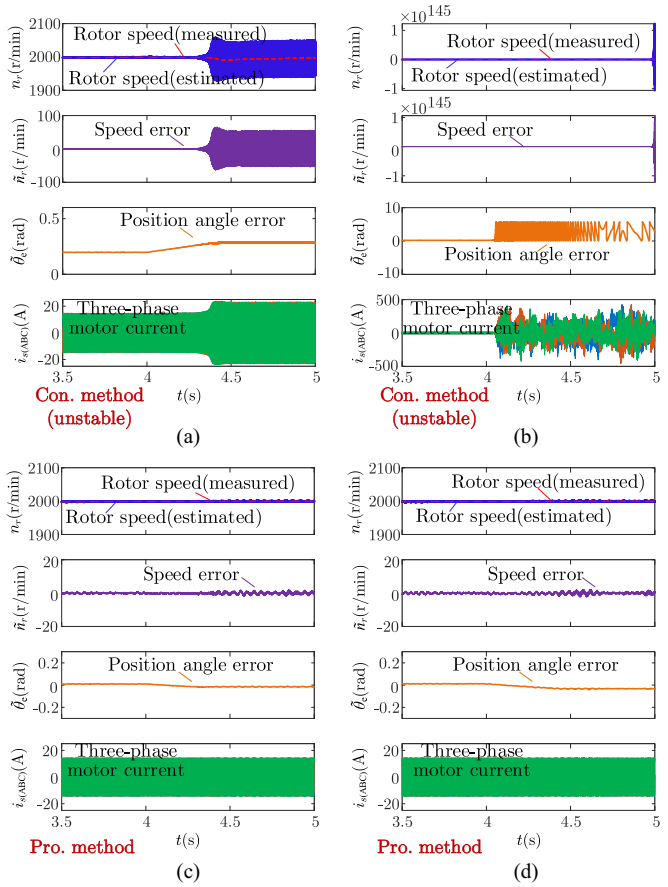

Fig. 10. Robustness test under parameters mismatch (parameter ramp mismatch given at 4 s, motor speed 2000 r/min and load torque 10 N·m). (a) Conventional model with ultimate estimated filter inductance L_f reduced to 50% of the actual value. (b) Conventional model with ultimate estimated filter capacitance C_f reduced to 33% of the actual value. (c) Proposed model with ultimate estimated filter inductance L_f reduced to 50% of the actual value. (d) Proposed model with ultimate estimated motor inductance L_s reduced to 50% of the actual value.

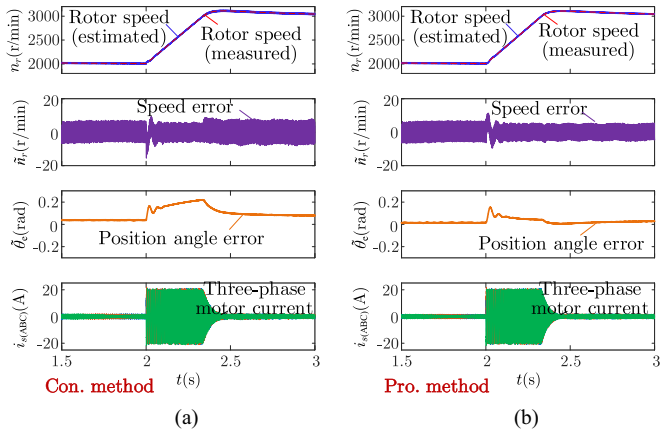

Fig. 11. Speed sensorless control performance comparison between conventional model and proposed reduced-order model under nonsinusoidal back-EMF case (rotor speed changes from rated 2000 to 3000 r/min). (a) Sensorless control based on conventional model. (b) Sensorless control based on the proposed model.

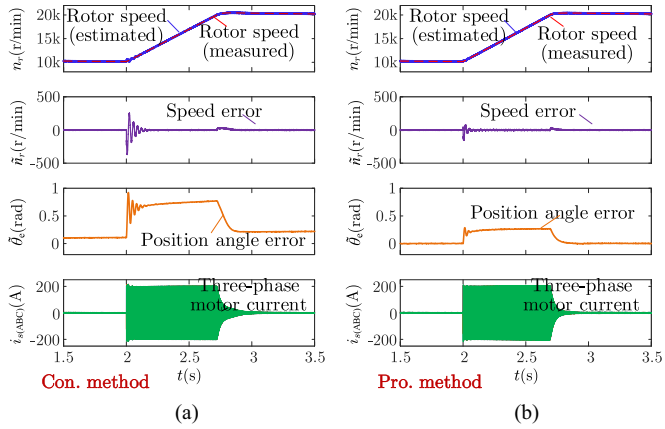

Fig. 12. Speed sensorless control performance comparison between conventional model and proposed reduced-order model for high-speed motor operation (rotor speed changes from 10 000 to higher speed 20 000 r/min). (a) Sensorless control based on conventional model. (b) Sensorless control based on the proposed model.

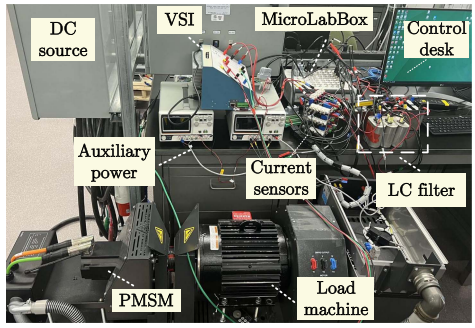

Fig. 13. Experimental setup of the SPMSM drive with LC filter.

TABLE I
PARAMETERS OF THE LC -FILTERED PMSM DRIVE SYSTEM

Parameters	Value
DC-link voltage	200V
DC-link capacitance	1.4mF
Rated torque	6N·m
Rated stator frequency	1000r/min
Number of pole pairs	5
Rotor flux linkage	0.15Wb
Stator resistance	0.2Ω
Stator inductance	3.1mH
Inverter-side inductance	3mH
Filter capacitance	10μF
Filter cut-off frequency	919Hz
Sampling frequency	10kHz

B. Experimental Verification

Fig. 13 shows a scaled-down experimental setup for the LC-filtered SPMSM with parameters given in Table I. A two-level VSI is configured by insulated-gate bipolar transistor power modules, and the dc voltage comes from the REGA-TRON

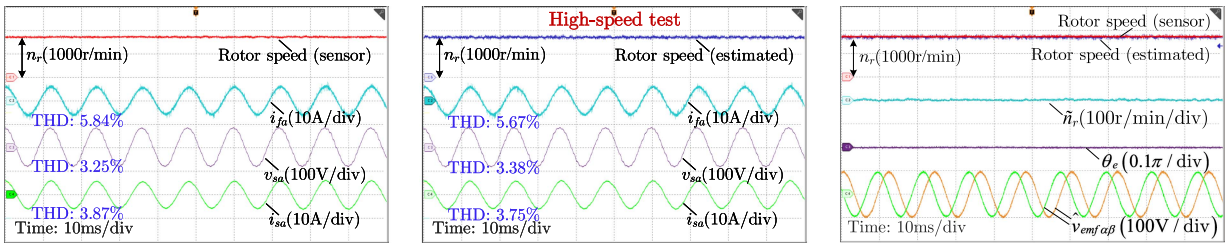

Fig. 14. Steady-state control performance based on real speed sensor and speed sensorless operation under the 1000 r/min rotor speed and 5 N·m load torque. (a) Real speed sensor-based control. (b) Proposed speed sensorless control. (c) Estimated EMF and the extracted speed and position error.

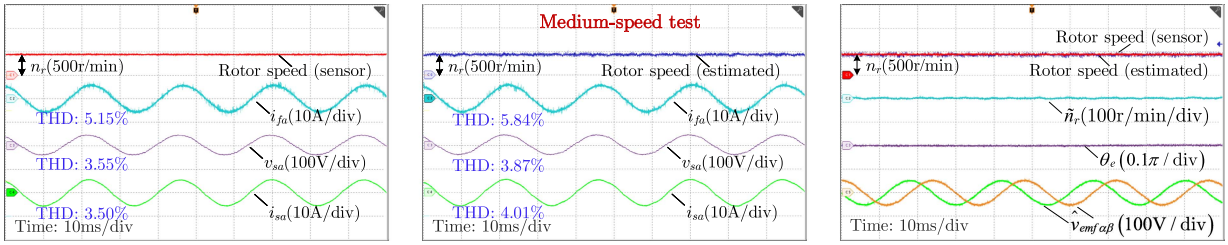

Fig. 15. Steady-state control performance based on real speed sensor and speed sensorless operation under the 500 r/min rotor speed and 5 N·m load torque. (a) Real speed sensor-based control. (b) Proposed speed sensorless control. (c) Estimated EMF and the extracted speed and position error.

programmable power source. The system is digitally controlled by the dSPACE MicroLabBox 1202 platform, and the SVPWM block is employed to generate the switching pulse based on the voltage command. The I-f open-loop method is used to start up the PMSM, after which it transitions to the effective operation range of the model-based speed-sensorless control, typically around 20% of the rated speed [39]. Based on SPMSM drive system parameters, the calculation results of the PI parameters are $k_p = 3.89$ and $k_i = 628$, where the cutoff frequency of the current loop is set as 200 Hz. The damping coefficient k_{AD} is set to 8.37 to emulate the 4.12 Ω virtual resistance. The open-loop transfer function demonstrates a stable response, ensuring a sufficient phase margin of 71° and a gain margin of 14.3 dB. The computational load of the Kalman filter observer, based on the proposed virtual reduced-order model, requires 21.48 μs to complete the interrupt tasks.

To verify the control performance using the proposed speed sensorless operation, the real speed sensor-based control performance is also implemented as the benchmark for comparison. Fig. 14 shows the steady-state control performance at a rotor speed (n_r) of 1000 r/min and 5 N·m load torque by using the real speed sensor and the proposed speed sensorless operation, respectively. It can be seen that the proposed speed sensorless operation achieves similar total harmonic distortion (THD) performance of inverter-side current, filter capacitor voltage, and motor stator current compared to the case that uses the real sensor. Notably, there are no obvious resonant oscillations in both cases by using the capacitor current feedback. Fig. 15 shows the steady-state control performance under the 500 r/min rotor speed and 5 N·m load torque by using the real speed sensor and proposed sensorless operation, respectively. Again, the proposed speed sensorless operation exhibits similar performance characteristics to the real speed sensor-based control. To assess the efficacy of the proposed model, the speed sensorless control strategy was evaluated at low operational speed, specifically at 20% of the nominal speed, which is a critical threshold for model-based sensorless control techniques. Fig. 16 depicts the steady-state performance of the control system under such conditions, with the rotor speed maintained at 200 r/min and a load torque of 2 N·m. Compared to the results obtained using the real speed sensor, the proposed sensorless operation consistently maintains stable performance metrics, akin to those achieved with sensor-based control case. Furthermore, Figs. 14(c) and 15(c) illustrates the estimated speed and position error for both 1000 and 500 r/min rotor speeds under the proposed sensorless control scheme. The sinusoidal EMF is estimated through the proposed virtual plant. Notably, the estimated speed closely aligns with the measured results obtained using the real sensor. Both the average estimated speed and position error are near zero, signifying the excellent performance achieved by the proposed approach. Fig. 16(c) details the estimated speed and position errors under low speed 200 r/min case, demonstrating that the proposed method effectively maintains an average zero speed estimation error and exhibits minor positional inaccuracies.

The dynamic performance of the proposed speed sensorless operation is verified in Figs. 17 and 18. Fig. 17 shows the cases when the rotor speed changes from 500 to 1000 r/min under no-load or with a load torque of 5 N·m, respectively. It can be seen that the acceleration process occurs smoothly without any resonance. While an increase in estimated error is

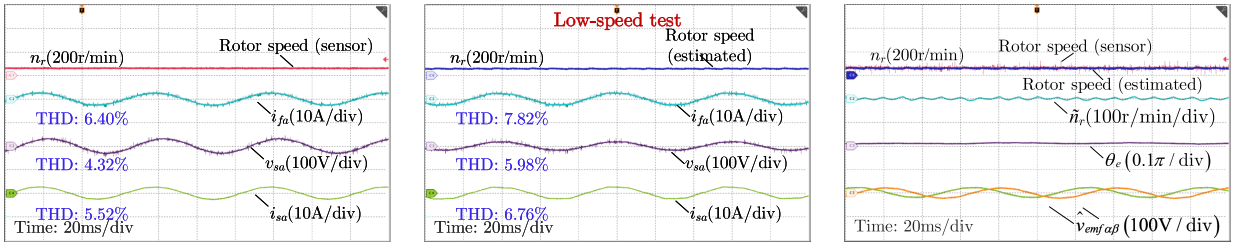

Fig. 16. Steady-state control performance based on real speed sensor and speed sensorless operation under the 200 r/min rotor speed and 2 N·m load torque. (a) Real speed sensor-based control. (b) Proposed speed sensorless control. (c) Estimated EMF and the extracted speed and position error.

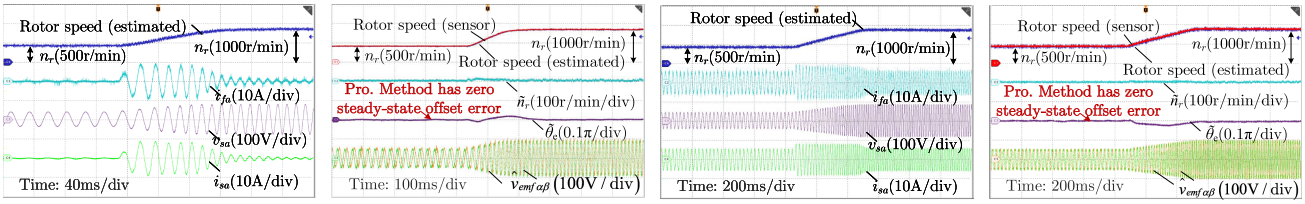

Fig. 17. Dynamic performance of the proposed speed sensorless control during a rotor speed change from 500 to 1000 r/min. (a) Dynamic performance of state variables with no load. (b) Estimated speed and position error and EMF corresponding to (a). (c) Dynamic performance of state variables with 5 N·m load. (d) Estimated speed and position error and EMF corresponding to (c).

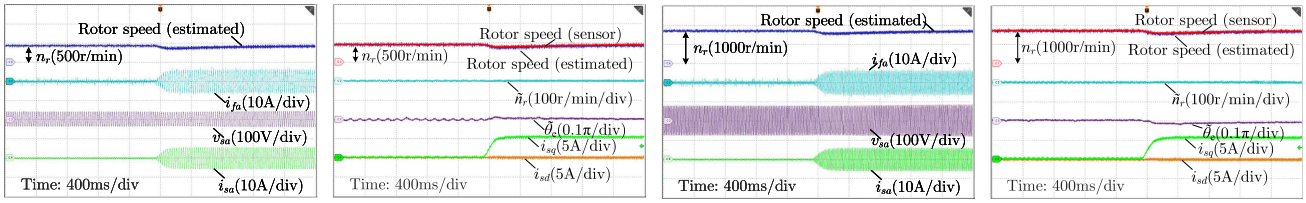

Fig. 18. Dynamic performance of the proposed speed sensorless control with load torque increase from 0 to 5 N·m. (a) Dynamic performance of state variables with 500 r/min rotor speed. (b) Estimated speed and position error and EMF corresponding to (a). (c) Dynamic performance of state variables with 1000 r/min rotor speed. (d) Estimated speed and position error and EMF corresponding to (c).

observed during this dynamic process, the estimation error for speed and position remains within acceptable limits, peaking at 15 r/min and 4°, respectively. Besides, the estimation error rapidly converges to zero as the system stabilizes at the new steady state. Therefore, the proposed speed sensorless operation presented good performance in terms of dynamic speed change. On the other hand, the case when dynamic load torque changes is given in Fig. 18 for both 500 and 1000 r/min. Again, the system performs well with a smooth change of dq-axes current. The proposed speed sensorless scheme shows a strong capability to reject the disturbance change, and the estimated error of speed is close to zero during the dynamic process. Besides, the estimated error of the position can be limited to 4°, which is acceptable for the speed sensorless operation.

Fig. 19(a) shows the estimated speed, position error, and EMF of the conventional method during a rotor speed change from 500 to 1000 r/min. In comparison, the estimated position angle error in Fig. 17(b) demonstrates that the proposed method achieves smaller estimation errors. In addition, when the conventional

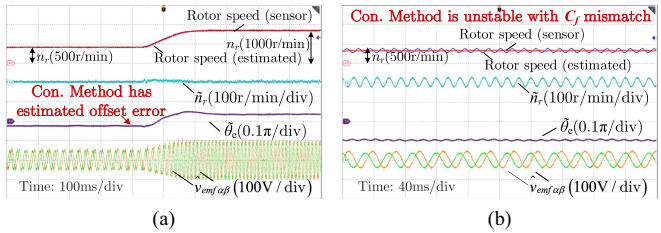

Fig. 19. Conventional model-based sensorless control. (a) Estimated speed and position error and EMF of conventional method with rotor speed change from 500 to 1000 r/min. (b) Estimated speed and position error and EMF of conventional method at 500 r/min. with estimated filter capacitance C_f reduced to 33% of the actual value.

method is tested with the estimated capacitance C_f reduced to 33% of its actual value, it becomes unstable, as shown in Fig. 19(b), highlighting its vulnerability to capacitance mismatch. In contrast, the proposed method, which does not rely on the capacitance parameter, remains robust and unaffected by this issue.

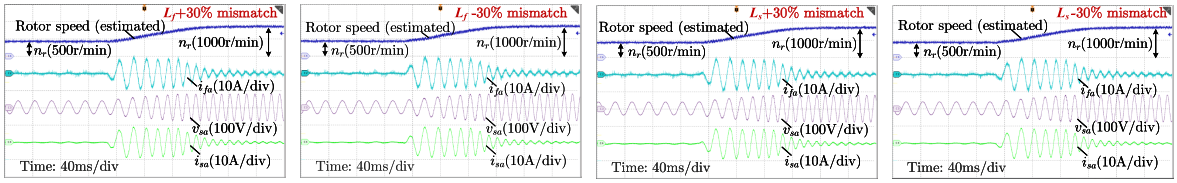

Fig. 20. Dynamic performance under the inductance mismatch (rotor speed changes from 500 to 1000 r/min. with no load). (a) L_f+30%. (b) L_f-30%. (c) L_s+30%. (d) L_s-30%.

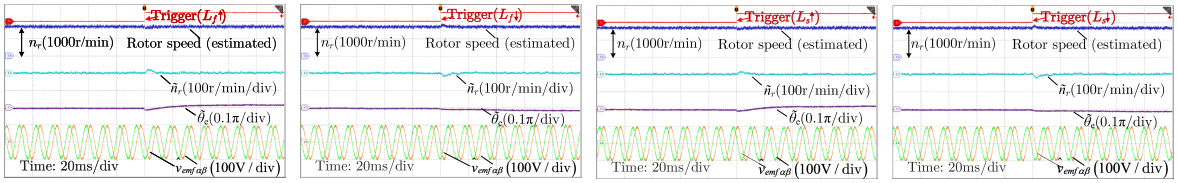

Fig. 21. Estimated error of speed and position under the inductance mismatch (rotor speed 1000 r/min. with 5 N·m load torque). (a) L_f+30%. (b) L_f-30%. (c) L_s+30%. (d) L_s-30%.

To assess the effectiveness of the proposed speed sensorless scheme in handling parameter variations, a $\pm$ 30% mismatch of the filter inductance and motor stator inductance is intentionally introduced during the controller's computational process. Fig. 20 shows the dynamic performance of the system with rotor speed command changes from 500 to 1000 r/min. It can be seen that the system keeps good stability and still achieves a similar performance compared to the standard case shown in Fig. 17. Therefore, the virtual plant-based observer guarantees stability in terms of inductance mismatch. Furthermore, the estimated error of speed and position under the steady-state case with 1000 r/min and 5 N·m load torque under the inductance mismatch is given in Fig. 21. It can be seen that the mismatch of the inductance will introduce a slight estimated error of position. However, the estimated error of speed can still be kept around zero, and the slight estimated error of position can be always maintained within 4°. Furthermore, the estimation error of position corresponds to the analysis given in Fig. 6. First, the increase of either the filter inductance or the motor stator inductance used in the control loop will cause an additional positive virtual inductance, as presented in Fig. 6(a). The increased inductance introduces more phase lag effect, and thus, the estimated EMF lags behind the real EMF, bringing the positive position estimation error. Conversely, the decrease in the inductance introduces the phase lead effect on the estimated EMF; thus, the estimation error will be slightly negative. It should be noted that since the most common tolerances of the LC filter are only within $\pm$ 10% around the nominal values provided by the manufacturers [40], the deliberately considered 30% mismatch is sufficient to verify the robustness of the proposed scheme.

V. Conclusion

This article proposed a virtual reduced-order plant-based back EMF modeling and speed sensorless operation for the PMSM drive system equipped with the LC filters. Considering this complex system with a strong coupling dynamic, the proposed solution achieves a satisfactory performance while maintaining a low complexity for both the design and computation stages. The AD function is designed into the FOC framework with proportional capacitor current feedback, and the well-designed feedback coefficient guarantees good steady-state performance and smooth dynamic performance without resonant oscillations. The proposed virtual plant-based back EMF equation turns the original third-order modeling into a first-order modeling; thus, avoiding the complex observer design for EMF estimation with the high-dimensional gain matrix. The well-developed observers for the drive system in the first-order formulation can be directly adopted, which offers a simplified design and tuning procedure, along with an intuitive robustness analysis. Besides, the proposed scheme offers the advantages of operating without voltage measurements and being independent of capacitor parameter, and the Kalman-filter-based EMF observer shows good stability and robustness to the mismatch in system inductance. As a result, the proposed approach can be a good application for PMSM drives with inverter-side output filters, where the high dv/dt is a critical concern.

Appendix

A. Matrices in the Original System Modeling

The matrices for the original dynamic (9) are given here

$$\mathbf{A_o} = \begin{bmatrix} -\frac{R_f}{L_f} & 0 & -\frac{1}{L_f} & 0 & 0 & 0 \\ 0 & -\frac{R_f}{L_f} & 0 & -\frac{1}{L_f} & 0 & 0 \\ \frac{1}{C_f} & 0 & 0 & 0 & -\frac{1}{C_f} & 0 \\ 0 & \frac{1}{C_f} & 0 & 0 & 0 & -\frac{1}{C_f} \\ 0 & 0 & \frac{1}{L_{sd}} & 0 & -\frac{R_s}{L_{sd}} & 0 \\ 0 & 0 & 0 & \frac{1}{L_{sd}} & 0 & -\frac{R_s}{L_{sd}} \end{bmatrix}$$

$$\mathbf{B_o}=\begin{bmatrix}\frac{1}{L_f} & 0\\ 0 & \frac{1}{L_f}\\ 0 & 0\\ 0 & 0\\ 0 & 0\\ 0 & 0\end{bmatrix}\quad \mathbf{E_o}=\begin{bmatrix}0\\ 0\\ 0\\ 0\\ \frac{1}{L_{sd}}\left(v_{eemf}\sin\theta_e-\omega_e L_\Delta i_{s\beta}\right)\\ \frac{1}{L_{sd}}\left(-v_{eemf}\cos\theta_e+\omega_e L_\Delta i_{s\alpha}\right)\end{bmatrix}.$$

B. Calculation Results of Kalman Filter Gain Matrix

The observer gain matrix by using the original high order model is calculated as follows:

$$\mathbf{K}_{\mathrm{oe}}(\infty)=\begin{bmatrix}0.3858 & 0.0001 & 0.0793 & -0.0001\\ 0.0003 & 0.3858 & -0.0001 & 0.0793\\ -0.9073 & -0.0003 & -1.7293 & 0.0003\\ -0.0020 & -0.9073 & 0.0044 & -1.7293\\ 0.0793 & 0.0001 & 0.7385 & -0.0000\\ -0.0001 & 0.0793 & 0.0008 & 0.7385\\ 0.7504 & 0.0037 & 4.8925 & -0.0017\\ 0.0094 & 0.7504 & -0.0099 & 4.8925\end{bmatrix}.$$

The observer gain matrix by using the proposed virtual reduced-order model is calculated as follows:

$$\mathbf{K}_{\mathrm{ve}}(\infty)=\begin{bmatrix}1.3840 & 0\\ 0 & 1.3840\\ -3.4361 & 0\\ 0 & -3.4361\end{bmatrix}.$$

REFERENCES

[1] A. Moreira, P. Santos, T. Lipo, and G. Venkataramanan, "Filter networks for long cable drives and their influence on motor voltage distribution and common-mode currents," *IEEE Trans. Ind. Electron.*, vol. 52, no. 2, pp. 515–522, Apr. 2005.

[2] J. He, G. Y. Sizov, P. Zhang, and N. A. Demerdash, "A review of mitigation methods for overvoltage in long-cable-fed PWM AC drives," in *Proc. 2011 IEEE Energy Convers. Congr. Expo.*, 2011, pp. 2160–2166.

[3] M. S. Diab and X. Yuan, "A quasi-three-level PWM scheme to combat motor overvoltage in SiC-based single-phase drives," *IEEE Trans. Power Electron.*, vol. 35, no. 12, pp. 12639–12645, Dec. 2020.

[4] L. Wang, C. Ngai-Man Ho, F. Canales, and J. Jatskevich, "High-frequency modeling of the long-cable-fed induction motor drive system using TLM approach for predicting overvoltage transients," *IEEE Trans. Power Electron.*, vol. 25, no. 10, pp. 2653–2664, Oct. 2010.

[5] O. Magdun and A. Binder, "High-frequency induction machine modeling for common mode current and bearing voltage calculation," *IEEE Trans. Ind. Appli.*, vol. 50, no. 3, pp. 1780–1790, Mar. 2014.

[6] A. Muetze and A. Binder, "Calculation of circulating bearing currents in machines of inverter-based drive systems," *IEEE Trans. Ind. Electron.*, vol. 54, no. 2, pp. 932–938, Feb. 2007.

[7] X. Yuan, I. Laird, and S. Walder, "Opportunities, challenges, and potential solutions in the application of fast-switching SiC power devices and converters," *IEEE Trans. Power Electron.*, vol. 36, no. 4, pp. 3925–3945, Apr. 2021.

[8] C. Xue, L. Ding, and Y. R. Li, "Model predictive control with reduced common-mode current for transformerless current-source PMSM drives," *IEEE Trans. Power Electron.*, vol. 36, no. 7, pp. 8114–8127, Jul. 2021.

[9] N. Parida and A. Das, "A modular multilevel converter with filter capacitor for long-cable-fed drive application," *IEEE Trans. Ind. Appli.*, vol. 55, no. 6, pp. 7833–7842, Jun. 2019.

[10] P. Mishra and R. Maheshwari, "Design, analysis, and impacts of sinusoidal LC filter on pulsewidth modulated inverter fed-induction motor drive," *IEEE Trans. Ind. Electron.*, vol. 67, no. 4, pp. 2678–2688, Apr. 2020.

[11] V. Dzhankhotov and J. Pyrhönen, "Passive lc filter design considerations for motor applications," *IEEE Trans. Ind. Electron.*, vol. 60, no. 10, pp. 4253–4259, Oct. 2013.

[12] C. Xue, D. Zhou, and Y. Li, "Finite-control-set model predictive control for three-level NPC inverter-fed PMSM drives with LC filter," *IEEE Trans Ind. Electron.*, vol. 68, no. 12, pp. 11980–11991, Dec. 2021.

[13] Z. Zhang, "Sensorless back EMF based control of synchronous PM and reluctance motor drives—a review," *IEEE Trans. Power Electron.*, vol. 37, no. 9, pp. 10290–10305, Sep. 2022.

[14] Y. Zuo, C. Lai, and K. L. V. Iyer, "A review of sliding mode observer based sensorless control methods for PMSM drive," *IEEE Trans. Power Electron.*, vol. 38, no. 9, pp. 11352–11367, Sep. 2023.

[15] G. Wang, M. Valla, and J. Solsona, "Position sensorless permanent magnet synchronous machine drives—a review," *IEEE Trans. Ind. Electron.*, vol. 67, no. 7, pp. 5830–5842, Jul. 2020.

[16] Y. Zhao, C. Wei, Z. Zhang, and W. Qiao, "A review on position/speed sensorless control for permanent-magnet synchronous machine-based wind energy conversion systems," *IEEE J. Emerg. Sel. Topics Power Electron.*, vol. 1, no. 4, pp. 203–216, Apr. 2013.

[17] A. Piippo, J. Salomaki, and J. Luomi, "Signal injection in sensorless PMSM drives equipped with inverter output filter," *IEEE Trans. Ind. Appli.*, vol. 44, no. 5, pp. 1614–1620, May 2008.

[18] Z. Chen, M. Tomita, S. Doki, and S. Okuma, "An extended electromotive force model for sensorless control of interior permanent-magnet synchronous motors," *IEEE Trans. Ind. Electron.*, vol. 50, no. 2, pp. 288–295, Feb. 2003.

[19] I. Boldea, M. C. Paicu, and G.-D. Andreescu, "Active flux concept for motion-sensorless unified ac drives," *IEEE Trans. Power Electron.*, vol. 23, no. 5, pp. 2612–2618, May 2008.

[20] J. Liu, T. A. Nondahl, J. Dai, S. Royak, and P. B. Schmidt, "A seamless transition scheme of position sensorless control in industrial permanent magnet motor drives with output filter and transformer for oil pump applications," *IEEE Trans. Ind. Appli.*, vol. 56, no. 3, pp. 2180–2189, Mar. 2020.

[21] H. Bu, I. Lee, J. Kim, B. Bae, D. Yoon, and Y. Cho, "Position sensorless control of long-cable-fed PMSM drive system using sine-wave filter," in *Proc. 11th Int. Conf. Power Electron. ECCE Asia (ICPE 2023 - ECCE Asia)*, 2023, pp. 934–940.

[22] Y. Xu, M. Wang, W. Zhang, and J. Zou, "Sliding mode observer for sensorless control of surface permanent magnet synchronous motor equipped with LC filter," *IET Power Electron.*, vol. 12, no. 4, pp. 686–692, Apr. 2019.

[23] J. Guzinski and H. Abu-Rub, "Sensorless induction motor drive with voltage inverter and sine-wave filter," in *Proc. 2013 IEEE Int. Symp. Sensorless Control Elect. Drives Predictive Control Elect. Drives Power Electron.* (SLED/PRECEDE), 2013, pp. 1–8.

[24] N. Vaishnav, N. K. Bajjuri, and A. K. Jain, "Inductor selection, improved active damping, and speed sensorless operation without voltage sensors in IM drive with LC filter," *IEEE Trans. Power Electron.*, vol. 37, no. 12, pp. 15272–15282, Dec. 2022.

[25] N. He et al., "Weighted average current control in a three-phase grid inverter with an LCL filter," *IEEE Trans. Power Electron.*, vol. 28, no. 6, pp. 2785–2797, Jun. 2013.

[26] C. Xue, X. Wu, and Y. Li, "Virtual reduced-order plant-based speed sensorless control for AC motor drives with output LC filter," in *Proc. 2024 IEEE Appl. Power Electron. Conf. Expo.* (APEC), 2024, pp. 1035–1040.

[27] W. Wu, Y. Liu, Y. He, H. S.-H. Chung, M. Liserre, and F. Blaabjerg, "Damping methods for resonances caused by LCL-filter-based current-controlled grid-tied power inverters: An overview," *IEEE Trans. Ind. Electron.*, vol. 64, no. 9, pp. 7402–7413, Sep. 2017.

[28] J. Dannehl, F. W. Fuchs, S. Hansen, and P. B. Thøgersen, "Investigation of active damping approaches for PI-based current control of grid-connected pulse width modulation converters with LCL filters," *IEEE Trans. Ind. Appli.*, vol. 46, no. 4, pp. 1509–1517, Apr. 2010.

[29] K. Hatua, A. K. Jain, D. Banerjee, and V. T. Ranganathan, "Active damping of output LC filter resonance for vector-controlled VSI-fed AC motor drives," *IEEE Trans. Ind. Electron.*, vol. 59, no. 1, pp. 334–342, Jan. 2012.

[30] K. Ito, R. Suzuki, K. Yoshimoto, and T. Yokoyama, "A study of multi-sampling deadbeat control for low carrier frequency PMSM drive system used in EVs and HEVs," in *Proc. 2021 IEEE Int. Conf. Mechatron. (ICM)*, 2021, pp. 1–6.

[31] Y. Tang, P. C. Loh, P. Wang, F. H. Choo, and F. Gao, "Exploring inherent damping characteristic of LCL-filters for three-phase grid-connected voltage source inverters," *IEEE Trans. Power Electron.*, vol. 27, no. 3, pp. 1433–1443, Mar. 2012.

[32] M. B. Saïd-Romdhane, M. W. Naouar, I. Slama-Belkhodja, and E. Monmasson, "Robust active damping methods for LCL filter-based grid-connected converters," *IEEE Trans. Power Electron.*, vol. 32, no. 9, pp. 6739–6750, Sep. 2017.

[33] J. He, Y. W. Li, D. Xu, X. Liang, B. Liang, and C. Wang, "Deadbeat weighted average current control with corrective feed-forward compensation for microgrid converters with nonstandard LCL filter," *IEEE Trans. Power Electron.*, vol. 32, no. 4, pp. 2661–2674, Apr. 2017.

[34] L. Wang, *Model Predictive Control System Design and Implementation Using MATLAB*. Berlin, Germany: Springer, 2009.
[35] S. Bolognani, L. Tubiana, and M. Zigliotto, "Extended Kalman filter tuning in sensorless PMSM drives," *IEEE Trans. Ind. Appli.*, vol. 39, no. 6, pp. 1741–1747, Jun. 2003.
[36] H. Wang, C. Li, G. Zhang, Q. Geng, and T. Shi, "Maximum torque per ampere (MTPA) control of IPMSM systems based on controller parameters self-modification," *IEEE Trans. Veh. Technol.*, vol. 69, no. 3, pp. 2613–2620, Mar. 2020.
[37] H. Wang, Y. Yang, X. Ge, Y. Zuo, Y. Yue, and S. Li, "PLL- and FLL-based speed estimation schemes for speed-sensorless control of induction motor drives: Review and new attempts," *IEEE Trans. Power Electron.*, vol. 37, no. 3, pp. 3334–3356, Mar. 2022.
[38] G. Wang et al., "Enhanced position observer using second-order generalized integrator for sensorless interior permanent magnet synchronous motor drives," *IEEE Trans. Energy Convers.*, vol. 29, no. 2, pp. 486–495, Feb. 2014.
[39] Z. Wang, K. Lu, and F. Blaabjerg, "A simple startup strategy based on current regulation for back-EMF-based sensorless control of PMSM," *IEEE Trans. Power Electron.*, vol. 27, no. 8, pp. 3817–3825, Aug. 2012.
[40] H. T. Nguyen, E.-K. Kim, I.-P. Kim, H. H. Choi, and J.-W. Jung, "Model predictive control with modulated optimal vector for a three-phase inverter with an LC filter," *IEEE Trans. Power Electron.*, vol. 33, no. 3, pp. 2690–2703, Mar. 2018.

Cheng Xue (Member, IEEE) received the B.Eng. (Hons.) and M.Sc. degrees in electrical engineering from Southwest Jiaotong University, Chengdu, China, in 2015 and 2018, respectively, and the Ph.D. degree in energy system from the Department of Electrical and Computer Engineering, University of Alberta, Edmonton, AB, Canada, in 2023.

From 2023 to 2025, he was a Postdoctoral Research Fellow with the Department of Electrical and Computer Engineering, University of Alberta. In 2025, he joined the School of Integrated Circuits Science and Engineering, Southwest Jiaotong University, China, as a faculty member. His research interests include advanced control, optimization and integration of power electronics converters for Microgrid applications and high-performance ac electrical machine drives.

Dr. Xue was the recipient of the Chinese Government Award for Outstanding Self-Financed Students Abroad in 2020, IEEE Transactions on Industrial Electronics Outstanding Reviewer Award twice (in 2022 and 2024) and also the 2023 Ph.D. Thesis Talk Award from the IEEE Power Electronics Society. His Ph.D. research was funded by the Alberta Province's Full-Service Innovation Engine "Alberta Innovates" from 2021 to 2022. He was recognized as the Distinguished Reviewer for IEEE TRANSACTIONS ON INDUSTRIAL ELECTRONICS for three consecutive years from 2021 to 2023. He was recognized as 2024 World's Top 2% Scientists ranked by Stanford University.

Xuesong Wu (Graduate Student Member, IEEE) received the B.Eng. (Hons.) and M.Sc. degrees in electrical engineering from Southwest Jiaotong University, Chengdu, China, in 2016 and 2019, respectively. He is currently working toward the Ph.D. degree in energy system with the Department of Electrical and Computer Engineering, University of Alberta, Edmonton, AB, Canada.

His research interests include electrical machine drives and grid-tied inverters.

Yuzhuo Li (Member, IEEE) received the B.S. and M.S. degrees in control science and engineering from Shandong University, Jinan, China, in 2012 and 2015, respectively, and the Ph.D. degree in energy system from the University of Alberta, Edmonton, AB, Canada, in 2021.

He is currently a Postdoctoral Fellow with the University of Alberta. His main research interests include intelligent and graph-based systematic power electronics design.

Yunwei (Ryan) Li (Fellow, IEEE) received the B.Sc. degree in electrical engineering from Tianjin University, Tianjin, China, in 2002, and the Ph.D. degree in electrical engineering from Nanyang Technological University, Singapore, in 2006.

In 2005, he was a Visiting Scholar with Aalborg University, Aalborg, Denmark. From 2006 to 2007, he was a Postdoctoral Research Fellow with Ryerson University, Toronto, ON, Canada. In 2007, he was with Rockwell Automation Canada before he joined the University of Alberta, in the same year. Since then, he has been with the University of Alberta, where he is a Professor and currently the Acting Department Chair. His research interests include distributed generation, microgrid, renewable energy, high power converters, and electric motor drives.

Dr. Li was the recipient of the Richard M. Bass Outstanding Young Power Electronics Engineer Award from the IEEE Power Electronics Society in 2013 and the 8th Nagamori Awards in 2022. He is currently the Vice President for products of IEEE Power Electronics Society. Prior to that, he was the Editor-in-Chief for IEEE TRANSACTIONS ON POWER ELECTRONICS LETTERS, an Associate Editor for IEEE TRANSACTIONS ON POWER ELECTRONICS, IEEE TRANSACTIONS ON INDUSTRIAL ELECTRONICS, IEEE TRANSACTIONS ON SMART GRID, and IEEE JOURNAL OF EMERGING AND SELECTED TOPICS IN POWER ELECTRONICS. He was the General Chair of IEEE Energy Conversion Congress of Exposition, in 2020. He is the AdCom Member with Large for IEEE Power Electronics Society 2021–2023. He is recognized as a Highly Cited Researcher by the Web of Science Group. He was selected as the Fellow of the Canadian Academy of Engineering in 2024.